Nanoscale

PAPER

View Article Online
View Journal | View Issue

Published on 11 November 2015. Downloaded by Los Alamos National Laboratory on 14/12/2016 00:33:04.

Cite this: *Nanoscale*, 2015, **7**, 20521

Photoluminescence imaging of solitary dopant sites in covalently doped single-wall carbon nanotubes†

Nicolai F. Hartmann,‡[a] Sibel Ebru Yalcin,‡[a] Lyudmyla Adamska,[a,b] Erik H. Hároz,[a] Xuedan Ma,[a] Sergei Tretiak,[a,b] Han Htoon[a] and Stephen K. Doorn*[a]

Covalent dopants in semiconducting single wall carbon nanotubes (SWCNTs) are becoming important as routes for introducing new photoluminescent emitting states with potential for enhanced quantum yields, new functionality, and as species capable of near-IR room-temperature single photon emission. The origin and behavior of the dopant-induced emission is thus important to understand as a key requirement for successful room-T photonics and optoelectronics applications. Here, we use direct correlated two-color photoluminescence imaging to probe how the interplay between the SWCNT bright E_{11} exciton and solitary dopant sites yields the dopant-induced E_{11}* emission for three different dopant species: oxygen, 4-methoxybenzene, and 4-bromobenzene. We introduce a route to control dopant functionalization to a low level as a means for introducing spatially well-separated solitary dopant sites. Resolution of emission from solitary dopant sites and correlation to their impact on E_{11} emission allows confirmation of dopants as trapping sites for localization of E_{11} excitons following their diffusive transport to the dopant site. Imaging of the dopant emission also reveals photoluminescence intermittency (blinking), with blinking dynamics being dependent on the specific dopant. Density functional theory calculations were performed to evaluate the stability of dopants and delineate the possible mechanisms of blinking. Theoretical modeling suggests that the trapping of free charges in the potential well created by permanent dipoles introduced by dopant atoms/groups is likely responsible for the blinking, with the strongest effects being predicted and observed for oxygen-doped SWCNTs.

Received 14th September 2015,
Accepted 10th November 2015

DOI: 10.1039/c5nr06343d

www.rsc.org/nanoscale

Introduction

Doping of semiconductor materials is a powerful and tunable means for modulating their optical, electronic, and magnetic properties. Examples of such tunability range across dimensionality from bulk 3-D[1] to low dimensional materials including 2-D quantum wells[2] and layered materials,[3,4] 1-D nanowires and carbon nanotubes,[5,6] and quasi 0-D systems, such as quantum dots[7] and substitutionally doped materials like nanodiamonds.[8] Control at the solitary dopant level is becoming increasingly important as a route to opening applications in spin-coupled optics,[7,8] spin-based devices, single-electron transistors, and development of non-classical light sources.[9] In particular, the ability of solitary dopants and defect states to introduce atomic-like states directly underlies their potential for creating single-photon emitters.[8,10–12] Observation of single photon emission at room-temperature (T) in such defect-based systems recently has been expanded to include 1-D semiconducting single-wall carbon nanotubes (SWCNTs).[13] While single photon emission in SWCNTs had been demonstrated previously at cryogenic temperatures,[14–16] only recently has this behaviour been realized at room-T, resulting from the ability to localize excitons at sp^3 defect centers introduced by low-level covalent functionalization.[13]

Introduction of sp^3 defects by covalent functionalization of the SWCNT surface *via* ozonation[5] (to generate ether or epoxide species) or reaction with aryl diazonium species[6] generates new photoluminescent states that emit from ~100 meV to as much as 300 meV lower in energy than the lowest energy (E_{11}) SWCNT exciton emitting state. Low-T spectroscopic studies[17] and T-dependent photoluminescence (PL) behavior of oxygen-doped SWCNTs[18] suggests a picture in which efficient diffusion of an optically excited exciton transports it to a dopant site. Deep traps introduced by the dopant then spatially localize the exciton. The associated dopant electronic

[a]*Center for Integrated Nanotechnologies, Materials Physics and Applications Division, Los Alamos National Laboratory, Los Alamos, New Mexico 87545, USA. E-mail: skdoorn@lanl.gov*
[b]*Theory Division, Los Alamos National Laboratory, Los Alamos, New Mexico 87545, USA*
†Electronic supplementary information (ESI) available. See DOI: 10.1039/c5nr06343d
‡Equal contribution.

Published on 11 November 2015. Downloaded by Los Alamos National Laboratory on 14/12/2016 00:33:04.

structure typically leads to a 4-level system with potential for lasing. Furthermore, consequences of the suggested exciton localization include extended PL lifetimes (to 100s of ps),[13,18] enhanced quantum yields,[5,6,18] altered saturation behavior and exciton–exciton annihilation processes.[17,19–21] Exciton localization is also a critical requirement for observation of single-photon emission.[14–16] The trapping potentials associated with the covalent SWCNT dopants have been shown recently to be sufficiently deep for demonstration of single photon emission at room-T.[13] Such a finding opens the possibility of electrically driven emission from the dopant sites and their use as quantum light sources required for quantum information processing at telecom wavelengths, as well as for novel photon sources for a variety of fundamental experiments in quantum optics.

Many of the applications envisioned for this new defect-based SWCNT emission will require fine control of doping densities, to the point of introduction of spatially well-isolated and even solitary dopants on individual SWCNTs. Additionally, despite the important consequences for optical behaviors arising from the proposed exciton localization and conversion at dopant sites, such a model is based on indirect behaviors that imply diffusive transport to and localization at these trapping sites.[17,18] A more direct demonstration of this behavior, however, remains lacking. Furthermore, the observation of single photon emission at room-T from individual dopant sites requires matrix stabilization of dopant-state emission.[13] The sources of emission instability are not yet understood, but must be established in order to design improved matrices for optimizing emission quality and minimizing sources of emission line broadening. Controlling the quality of emission from dopant states is the key to prospective use of functionalized SWCNTs as sensors[22] or single-photon light sources.[13]

Here, we demonstrate the ability to introduce single or well-separated, spatially resolvable few dopants per SWCNT. Such control over dopant density allowed us to implement a correlated 2-color PL imaging technique, with which we image individual dopant sites on ozonated and aryl diazonium functionalized SWCNTs. This probing of the dopant sites and their interaction with E_{11} excitons directly demonstrates exciton localization at trap sites following diffusive transport to these sites. Results supporting this model are consistent for both classes of dopants studied here. Finally, we also observe blinking of dopant emission at individual sites. Pairing of observed blinking dynamics with quantum chemical modelling of the dopant sites leads to the conclusion that blinking arises from localized charging events.

Materials and methods

Doped single-chirality SWCNT sample preparation

HiPCo (Rice University, HPR195.3) SWCNTs were dispersed in a 1.04% (w/v) sodium deoxycholate (DOC, AMRESCO, Lot#: 0331C075) solution in nanopure H_2O (18.3 MΩ cm) by stirring for 1 month at room temperature.[23] Subsequently the suspension was directly chirality sorted for (6,5) SWCNTs following an aqueous two-phase separation procedure described in ref. 24 without subjecting the suspension to ultracentrifugation. For the first separation step 201.1 mg of the DOC/SWCNT dispersion, 420.5 mg nanopure H_2O (ρ = 18.3 MΩcm) and 4.243 g STOCK-I solution (14.1 g polyethyleneglykol (PEG, MW 6000 Da, Alfa Aesar. Lot#: 10173268), 4.9 g dextran (MW 64000–76000 Da, Sigma Aldrich, Lot#: 091M1434 V), 0.49 g sodium cholate (SC, Sigma Aldrich, Lot#: 040M0156), 1.117 g sodium dodecylsulfate (SDS, Sigma Aldrich, Lot#: C1254) per 100 g nanopure H_2O) were thoroughly mixed *via* a vortex mixer and subsequently centrifuged for 5 min at 6000 *g* in a fixed angle centrifuge (Thermo-Electron 1EC MultiRF) to accelerate separation of the PEG- and dextran-rich phases. After centrifugation the purple colored bottom phase was extracted with a syringe and mixed with an equal amount of STOCK-II solution (2.33 g dextran, 14.5 g PEG, 0.0473 g DOC and 1.8 g SDS per 100 g nanopure H_2O) for the second separation step. The solution was thoroughly vortexed, cooled for 20 min in an ice-bath and then centrifuged for 5 min at 6000*g*. This results in a purple top phase and a nearly transparent bottom phase. The top phase is extracted, followed by removal of excess PEG and dextran *via* a pressure filtration/stirring cell (Millipore Amicon Stirred Cell) equipped with a regenerated 100 kDa cellulose membrane (Millipore Ultracel) and 1.04% (w/v) DOC solution as eluate. After this cleaning step the separated (6,5) suspension was dialysed into 1.0% (w/v) sodium dodecylbenzenesulfonate (SDBS, Sigma Aldrich, Lot#: 04710CE) through dialysis cassettes (Slide-A-Lyzer G2, 20 000 MWCO) at 60 °C solution temperature and constant stirring.

For oxygen doping, the method introduced by Ghosh *et al.*[5] was slightly modified. Separated (6,5) SWCNTs in 1.0% (w/v) SDBS (OD of 0.04 at E_{11}) were diluted with nanopure H_2O to a concentration of 0.2% (w/v) SDBS. Ozonated nanopure H_2O (3 min O_3-flow through 20 mL nanopure H_2O at 0.2 kg cm^{-1} and 8.0 V, DEL OZONE LG-7 ozone generator) was then added with a volume ratio of 1 : 1. The reaction mixture was illuminated for 4 h by a quartz-tungsten halogen lamp (Thorlabs, QTH10) and subsequently quenched by pressure filtration through a 100 kDa cellulose membrane using 1.04% (w/v) DOC solution as eluate.

Doping with different diazonium salts was achieved by following an adapted method introduced by Piao *et al.*[6] A solution of 9.69 mmol L^{-1} 4-methoxybenzenediazonium tetrafluoroborate (MeO-Dz, Sigma Aldrich, Lot#: STBC6632 V) or 7.39 mmol L^{-1} 4-bromobenzenediazonium tetrafluoroborate (Br-Dz, Sigma Aldrich, Lot#: MKBK8511 V) in nanopure H_2O, further diluted 1 : 99, was added to the separated (6,5) SWCNTs in 1.0% (w/v) SDBS (OD 0.04 at E_{11}) in small 1–2 μL quantities. Once the desired doping level was reached through observation in a spectrofluorometer (Horiba Nanolog) the reactions were quenched by pressure filtration through a 100 kDa cellulose membrane using 1.0% (w/v) DOC solution as eluate. For adjustment of the solution pH value, NaOH (1.0 N, Sigma Aldrich, Lot#: 0.3920EA) solution was added until the desired pH value was reached.

 This journal is © The Royal Society of Chemistry 2015

Published on 11 November 2015. Downloaded by Los Alamos National Laboratory on 14/12/2016 00:33:04.

For microscopy, tetramethylorthosilicate (TMOS)/SWCNT gel samples were prepared. 100 μL of the final doped SWCNT solution in 1% (w/v) DOC were thoroughly mixed with 10 μL TMOS (Sigma Aldrich, Lot#: 14628TD).[25,26] 10 μL of this mixed solution were transferred onto quartz cover slips (ESCO optics, R525025) and a second cover slip was placed on top to sandwich the solution. After an average of 2–3 h the gelation progressed enough to stop diffusion of individual SWCNTs and constant imaging conditions could be achieved.

Optical microscope setup and dual color imaging

For dual color imaging, a standard inverted microscope (Olympus X71) equipped with an oil immersion objective (Olympus, UApo N 100×/NA = 1.49) was used. A 705 nm long pass beam splitter (Semrock, FF705-Di01) separates the 568 nm continuous wave laser excitation (Coherent Sapphire 568) from the photoluminescence (PL) emission signal. In order to achieve wide-field illumination the collimated laser output (2 mW before the beam splitter) was focused onto the back focal plane of the objective, resulting in a ~40 μm^2 uniform excitation region on the sample. The detected PL signal was divided by a 50 : 50 beam splitter (Thorlabs, BSW11) into the two imaging channels, each using a 900 nm long pass filter to further block any residual laser light. After filtering with a 980 nm band pass filter (10 nm FWHM, Thorlabs, FB980-10) the E_{11} detection channel was recorded on an electron-multiplying charge-coupled device camera (Princeton Instruments, EMPro 512 × 512 px). For detection of the E_{11}* channel the signal was filtered by a 1064 nm long pass (Semrock, 1064 nm Edge Basic) and recorded with a 2 dimensional InGaAs array detector (Princeton Instruments, OMA-V 320 × 256 px). The real-space image size on both detectors was kept equal *via* focusing the split, collimated PL signal with equivalent lenses (f = 1000 mm) onto the detectors. Both cameras were externally triggered, thus enabling synchronized recording of image series on both channels with an equal integration time of 1 s per frame. Due to the different camera pixel sizes and resolution the recorded image series were afterwards rescaled and overlaid with ImageJ.[27]

Theoretical modelling

Theoretical modelling of the doped SWCNTs was done using Density Functional Theory (DFT) as implemented in the Gaussian 09 software suite.[28] Atomic structure visualization was done with Avogadro[29] software and contour plots of electrostatic potential were prepared with the XCrysDen[30] package. Calculations were conducted for finite size (6,5) SWCNTs of 1.5 nm and 8 nm length. The SWCNT ends were terminated by hydrogen atoms following ref. 31 and one dopant was added in the middle of the SWCNT.[17] The atomic structure of doped nanotubes in the vicinity of the defects is shown in Fig. S4 (ESI†).

Electrostatic potentials were computed for 8 nm long SWCNTs using the B3LYP[32] functional and a minimal STO-3G basis set. Diffusion activation energies were calculated for 1.5 nm long CNTs with the B3LYP model and 6-31G basis set. In the latter case, solvation effects were included in the framework of the Conductor-like Polarizable Continuum Model (CPCM), with water as solvent. The diffusion activation energies were evaluated using transition state theory[33] as implemented in Gaussian 09 package.[28] All structures were geometry optimized using DFT with a root mean square force criterion of 10^{-5}.

Results and discussion

Single site SWCNT doping and imaging

Achieving single dopant site detection requires SWCNTs to be longer than the spatial resolution limit (500 nm) of the PL imaging system and control of the concentration of dopants to a level of about 1–2 sites per μm of SWCNT length. We studied long (6,5) SWCNTs (μms long) obtained by combining capability for chirality sorting *via* an aqueous two phase separation route[24,34,35] with one enabling the isolation of long SWCNTs,[23] while generating SWCNT systems amenable to a controlled doping protocol.

The use of stirred suspensions (as opposed to sonicated SWCNT material) is critical for generating sufficient numbers of nanotubes with lengths exceeding 2 μm within an ensemble also containing many shorter nanotubes. Our data analysis is performed on SWCNTs whose lengths typically range from 2 to 6 μm. Exchange of the separation media to a 1% SDS or 1% SDBS environment allows efficient access to the nanotube surfaces by our reactive dopant species. We monitored the progress of the doping reaction by comparing the E_{11} exciton PL emission intensity to that of the dopant emission (designated here as E_{11}*), allowing us to choose the point at which the extent of the reaction is halted. The reaction is quenched by pressure filtration of the SWCNT/dopant solution into a 1% DOC matrix. Exchange of SDS or SDBS by DOC at the SWCNT surface provides a surface structure that protects the SWCNT against further access and reaction by the dopants. This provides fine control over the extent of reaction, while permitting use of dopant concentrations that are sufficiently high to ensure rapid functionalization of the nanotubes. To obtain well-separated dopant sites along the SWCNT length, we halt the reaction at a point where the E_{11} to E_{11}* PL peak intensity ratio approaches ≈3 : 1 to 5 : 1. Fig. 1 shows typical ensemble PL spectra of (6,5) SWCNTs before and after functionalization with MeO-Dz in SDS, for which the E_{11} PL peak appears at 985 nm and the E_{11}* dopant peak appears at 1120 nm. We note that the E_{11} emission intensity for the lightly doped nanotubes is reduced somewhat, compared to that for the undoped sample. This is consistent with some loss in E_{11} intensity expected upon doping,[5] even at the low dopant densities applied here. After surfactant exchange into DOC both emission peaks are shifted by ≈5 nm to longer wavelengths. Dopant emission in the cases of oxygen and Br-Dz appears at 1123 and 1132 nm in a DOC surfactant environment, respectively. Additional features in the spectra of both undoped and doped nanotubes appear as a shoulder at ~1010 nm, a peak at ~1110 nm, and a weak feature at ~1200 nm. These correspond

Published on 11 November 2015. Downloaded by Los Alamos National Laboratory on 14/12/2016 00:33:04.

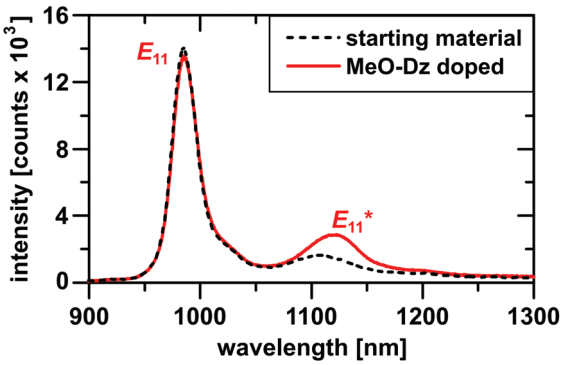

Fig. 1 As-obtained PL spectra of (6,5) SWCNTs before (black dashed line) and after functionalization with MeO-Dz (red solid line) in 1% SDS surfactant dispersion.

to phonon sidebands due to the radial breathing mode,[36] K-momentum dark exciton–phonon coupling,[37] and higher-order combination modes,[38] respectively.

Fig. 2(a–c) shows representative single tube PL images (additional examples given in Fig. S1 ESI†) for each of our three dopants, in which the E_{11}* dopant emission (red) is combined with E_{11} exciton emission images (green) to form a single spatially correlated PL image. We note that the E_{11}* emission appears as isolated emission spots overlaid on the more spatially continuous E_{11} emission. Furthermore, spatially correlated emission spectra obtained along the length of individual undoped nanotubes show only E_{11} emission features (see Fig. S2(a), ESI†). However doped SWCNTs show only E_{11} emission features in areas at which no dopant sites are found, while E_{11}* emission features are obtained only from positions at which dopant emission is observed in our wide-field PL images (see Fig. S2(b), ESI†). The observation of isolated, resolvable, dopant emission sites demonstrates our ability to functionalize the SWCNTs to the solitary dopant limit and represents the first imaging of such single dopant sites along a SWCNT surface. The appearance of dopant emission at isolated single sites supports the model of the associated sp^3 defects acting as a localized exciton trap. This idea is further supported by directly comparing the spatial behavior of the E_{11}* emission with that from the E_{11} exciton.

Fig. 2(d–f) displays spatially correlated intensity distributions of the E_{11}* (red traces) and E_{11} (green traces) PL along the length of the SWCNT examples shown in Fig. 2(a–c) (as determined along the overlaid dashed arrow). For these three examples, the position of maximum E_{11}* emission intensity at each dopant site correlates strongly with a collocated minimum in E_{11} emission intensity (additional examples given in Fig. S1 ESI†). We find this correlation is a general behaviour observed for all dopant types, and is observed for every occurrence of dopant emission (with a total sampling over all three dopants of 63 dopant sites across 59 individual tubes sampled). There are additional instances of quenched E_{11} emission sites at locations where no E_{11}* emission is observed. These cases may occur at sites in which a permanent structural defect exists, thus acting as a nonradiative exciton quenching center.[39] Alternatively, these sites may also be functionalized, but exhibit quenching of the trap-site emission as well, potentially linked to the PL blinking behavior discussed below.

Our consistent observation of E_{11} intensity loss at all dopant emission sites strongly supports the model of trapping of a photoexcited exciton, accompanied by its conversion to the electronic structure and emission properties associated with a specific sp^3 defect. If instead of this exciton-to-trap site conversion, a direct optical excitation of the dopant emission were to occur, one would instead expect to observe a superposition of dopant emission on a spatially continuous bright emission from E_{11} excitons, which is not found. The absence of this behavior argues against direct optical excitation of trap

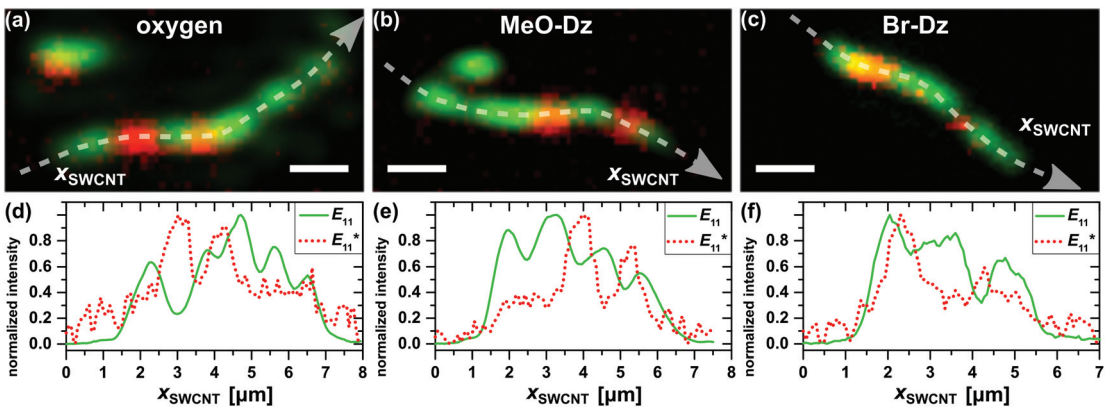

Fig. 2 Representative two channel PL images from ozone doped (a), MeO-Dz doped (b) and Br-Dz doped (c) individual SWCNTs. The images show the single dopant E_{11}* emission sites (red channel) distributed along the pristine E_{11} emission (green channel) of the SWCNTs. The scale bar represents 1 μm in all images. Corresponding intensity cross sections along the SWCNT axes x_{SWCNT}, as indicated by the white dashed line in (a–c), are shown in the second row for the ozone doped (d), MeO-Dz doped (e) and Br-Dz doped (f) SWCNT. A clear anti-correlation between E_{11} and E_{11}* emission is visible.

 This journal is © The Royal Society of Chemistry 2015

Published on 11 November 2015. Downloaded by Los Alamos National Laboratory on 14/12/2016 00:33:04.

sites being a dominant mechanism for generating the E_{11}^* emission in our experiments.

Diffusive transport of E_{11} exciton to dopant site

Another key aspect of the dopant-emission model is that exciton conversion to the electronic structure and emitting behavior of a dopant site is first preceded by its efficient diffusive transport to and trapping at the site. In order to further consolidate this aspect of our model, the intensity fall-off of the E_{11} emission associated with the dopant sites must be shown to be consistent with diffusive transport to the site. To do so, we begin by fitting the PL profiles of E_{11} emission for each individual SWCNT with a function based on 1D diffusion,[40] from which we extracted the exciton diffusion lengths.

The dopant sites were included in the model as point defect quenching centers which can be described by a double exponential function:[39,41]

$$I_{\text{defect}} = I_{0,\text{defect}} \mathrm{e}^{\frac{2|x_{\text{SWCNT}} - x_{\text{defect}}|}{\Lambda_{\text{D}}}} \quad (1)$$

Each defect along the SWCNT axis x_{SWCNT} is defined by a quenching amplitude $I_{0,\text{defect}}$, its position x_{defect} and an effective quenching range Λ_{D} connected to the exciton diffusion length following the definition of Siitonen *et al.*:[41]

$$\Lambda_D = 2l_{\text{D}} = 2\sqrt{D\tau}, \quad (2)$$

where D is the exciton diffusion coefficient and τ the intrinsic exciton lifetime.

For the E_{11} emission profile modelling, each defect site i quenches the undisturbed PL intensity distribution I_{SWCNT} obtained from the 1D diffusion:[40]

$$I_{\text{theo}}(x_{\text{SWCNT}}) = I_{\text{SWCNT}}(x_{\text{SWCNT}}, y_0, I_0, L, l_{\text{D,left}}, l_{\text{D,right}}) - \sum_i I_{\text{defect},i}(x_{\text{SWCNT}}, I_{0,i}, x_{\text{defect},i}, \Lambda_{\text{D},i}) \quad (3)$$

here x_{SWCNT} is the SWCNT axis, y_0 is a dark count correction, I_0 is intensity amplitude of the undisturbed SWCNT emission, L is the physical SWCNT length and $l_{\text{D,left}}/l_{\text{D,right}}$ are the exciton diffusion lengths for the left and right ends, respectively. In order to represent the experimental detection conditions, the theoretical intensity profile I_{theo} was then convoluted with a Gaussian function approximating the point-spread function (PSF) given by the microscope setup:

$$I_{\text{fit}}(x) = \mathrm{e}^{-\frac{1}{2}\left(\frac{x}{\sigma}\right)^2} \times I_{\text{theo}} \quad (4)$$

The Gaussian width σ is determined by fitting the Gaussian function to every individual intensity profile perpendicular to the SWCNT axis in order to account for any slight defocus and is on average σ = 210 nm.

Fig. 3(a–c) depicts three representative E_{11} PL intensity distribution profiles fitted according to eqn. (4) for oxygen (a), MeO-Dz (b) and Br-Dz (c) doped SWCNTs. The model gives excellent fits to the intensity variations observed along the SWCNT lengths and allows extraction of a unique l_{D} associated with each observed quenching site (those associated with emitting E_{11}^* sites, dark sites, and also including quenching at tube ends). Shown in blue in Fig. 3(d–f) are histograms of l_{D} values associated with all E_{11}^* emission sites for each of the three dopants obtained over a large number of individual tubes. We find for these sites an average l_{D} of 200 ± 126 nm. Included in these histograms are l_{D} occurrence rates (in red) obtained for non-emitting sites observed in the same collection of individual SWCNTs, with l_{D} values of 211 ± 129 nm comparing closely to those associated with the E_{11}^* emitting sites. Additionally, we obtain l_{D} values associated with E_{11} quenching at the tube ends ($l_{\text{D,left}}$ and $l_{\text{D,right}}$ combined), again finding similar results (see Fig. S3 (ESI†)). Finally, we note that the various l_{D} values obtained for our functionalized SWCNTs are all in close agreement with typical E_{11} diffusion length values reported in the literature.[40–42]

The close agreement between the l_{D} values associated with the E_{11}^* emitting sites and those associated with other types of quenching centers strongly indicates diffusive transport of E_{11} excitons to dopant sites as the initial step in the dopant emission mechanism. Thus, the strong spatial correlation between E_{11}^* emitting sites and E_{11} quenching, paired with the l_{D} analysis at dopant sites, gives comprehensive and self-consistent support to the model for excitation and emission from dopant states. This mechanism can now be conclusively described as beginning with optical excitation of E_{11} excitons, followed by diffusive transport to dopant sites where the exciton is trapped and adopts the electronic structure introduced by the specific dopant, ultimately associated with the E_{11}^* emission behavior.

E_{11}^* point emitters and exciton localization

Trapping of the E_{11}^* exciton directly implies localization at the dopant site, as suggested by our observation of isolated E_{11}^* emission spots. To establish such localization quantitatively, we also analyzed the 2-dimensional spatial distribution of light emission from the trap sites. E_{11}^* emission spots were fitted to 2D Gaussians for every frame in our imaging movies, with results then averaged over all frames for each spot. Values for the Gaussian width along (x_{SWCNT}) the SWCNT axis and perpendicular to (y_{SWCNT}) the SWCNT axis (as defined in the inset of Fig. 4(a) are then extracted and plotted against each other (Fig. 4(a and b)).

Theoretical results[17] give an expectation that localization on the scale of the dopant excited-state wavefunction will be ≈2–5 nm, depending on the exact dopant. In such a case, FWHM(x) should equal FWHM(y). Such an exact correspondence is given as the black dashed line in Fig. 4(a and b), with the PSF of our imaging system represented by FWHM(y) in these plots. We find the expected correspondence between our imaging resolution and observed lateral intensity spread of the dopant emission along the tube axis. The imaging results thus provide direct evidence for exciton localization at the dopant sites, within the constraints of our diffraction-limited spatial resolution.

The above discussion assumes that the observed E_{11}^* emission spots truly originate from solitary dopant sites. There is,

Published on 11 November 2015. Downloaded by Los Alamos National Laboratory on 14/12/2016 00:33:04.

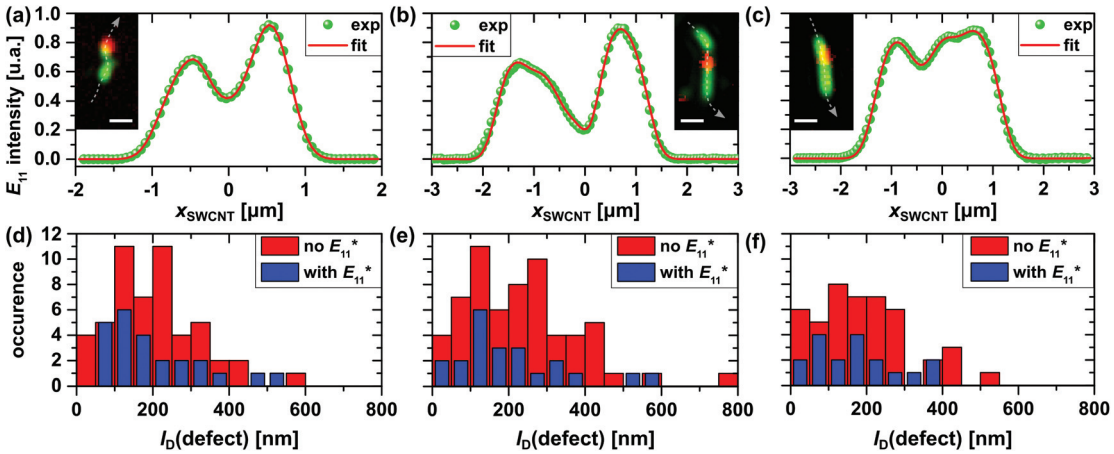

Fig. 3 Representative fits (red solid line) of E_{11} PL profiles (green dots) of oxygen doped (a), MeO-Dz doped (b) and Br-Dz doped (c) SWCNTs. The insets show the dual color images of the specific SWCNTs together with the indicated profiles (white dashed line). All scale bars represent 1 μm. (d)–(f) show histograms with the same *y*-axis scaling of l_D extracted from fits to multiple tubes doped with respective dopants. The red bars represent sites with no detectable E_{11}* emission and the blue bars sites with E_{11}* intensity present.

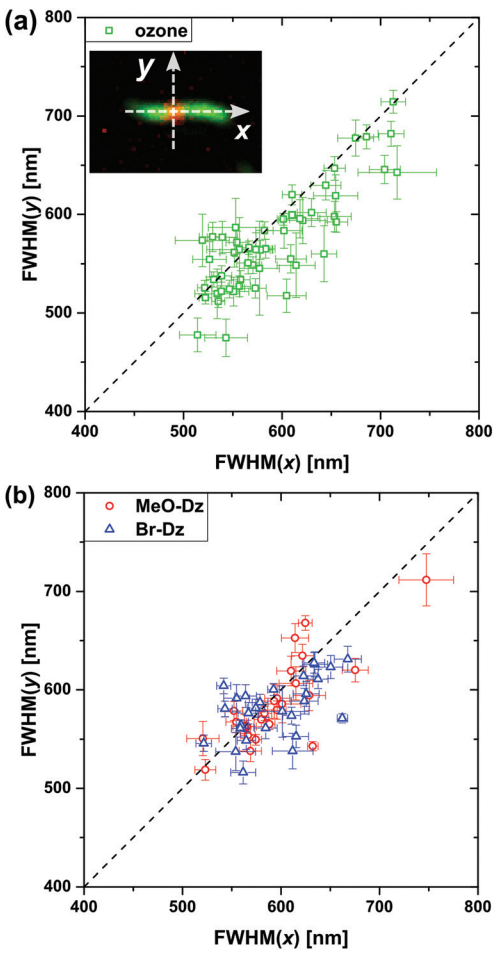

Fig. 4 Results of 2D Gaussian imaging widths in transverse (FWHM(*y*)) and axial (FWHM(*x*)) directions (as defined by image in inset to (a)) at individual dopant sites for oxygen doped (green points) (a) and MeO-Dz (red points) and Br-Dz (blue points) doped SWCNTs (b). The black dashed line indicates a direct *y* = *x* correlation in both plots.

however, a possibility for multiple dopants to exist close enough to each other to be imaged as unresolved emitting sites. We can, however, detect such instances as a result of blinking exhibited by the dopant emission (discussed in full in the next section), equivalent to the approach used in single molecule localization experiments.[43] Two sites separated within the diffraction limit become apparent when one site blinks independently of the other. An example is shown in Fig. 5(a–c), showing how the individual sites are resolvable when its counterpart blinks off. The accuracy of the position determination *via* a 2D Gaussian center of mass fit is about ±20 nm for the presented data.[44] We note that in the majority of instances in which an E_{11}* emission site is observed, its blinking behavior indicates it is a truly isolated single dopant site. The observed blinking behavior thus provides additional evidence that truly solitary dopant sites can indeed be created on the nanotube surface.

E_{11}* blinking dynamics

In acquiring the PL image data, we noted that the dopant emission often fluctuates, blinking between emission On and Off states. Because potential applications require stable emission sources, it is important to understand the origins of the blinking and how its behaviour depends on dopant species and environment. Example PL intensity time traces (red) exhibiting the E_{11}* blinking are shown in Fig. 6(a) and (b) for oxygen and methoxy-aryl dopants, respectively (movies showing blinking examples are available in the ESI†).

We note the dopant intensities fluctuate between On and Off states, while E_{11} PL intensities (green traces) do not blink. The contrasting E_{11} behaviour indicates the E_{11}* blinking is localized and solely associated with the dopant site.

Qualitative differences in blinking behaviour occur between the various dopants. In Fig. 6(a), blinking appears more quickly and more frequently for oxygen dopants, while for the

 This journal is © The Royal Society of Chemistry 2015

Published on 11 November 2015. Downloaded by Los Alamos National Laboratory on 14/12/2016 00:33:04.

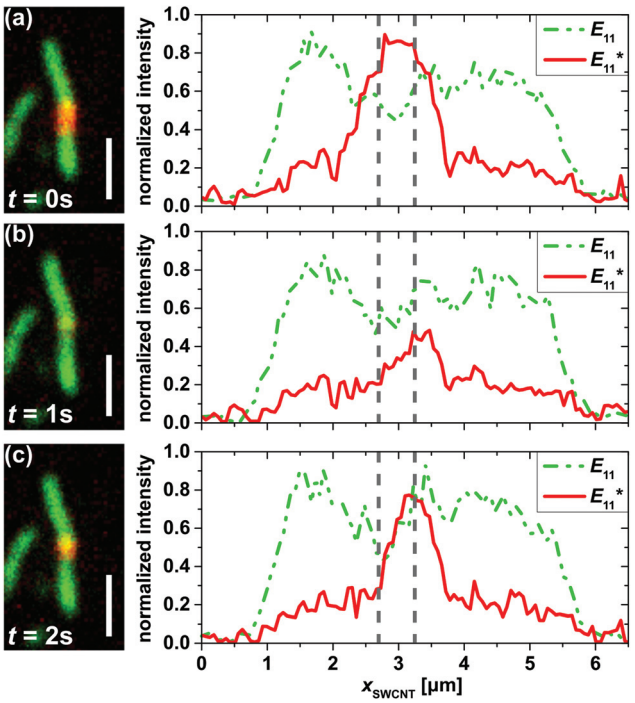

Fig. 5 Dual color images of a single MeO-Dz doped SWCNT at 0 s (a), 1 s (b) and 2 s (c) showing blinking of two individual dopant sites localized next to each other. During this time series the width of the E_{11}* emission spots changes as emphasized on the right hand side intensity distribution plots. The position of the two emission sites is indicated by the grey dashed lines, separated by 500 nm.

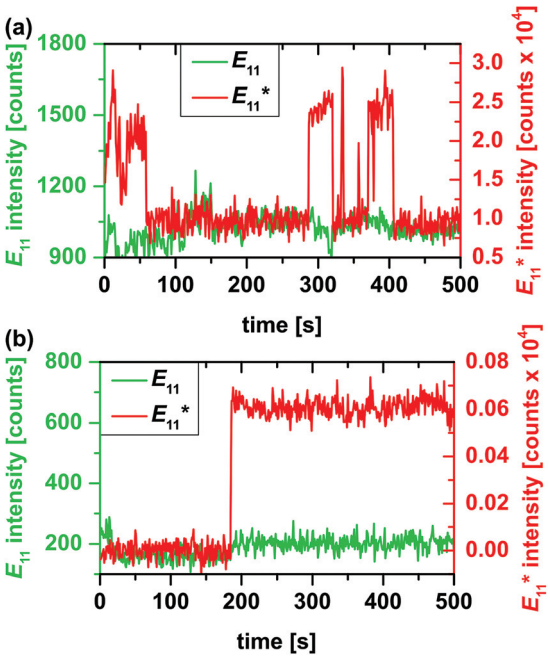

Fig. 6 Representative intensity traces over time for a single oxygen (a) and MeO-Dz dopant site (b). E_{11} intensity traces (green solid line) are overlaid with the E_{11}* intensity traces (red solid line).

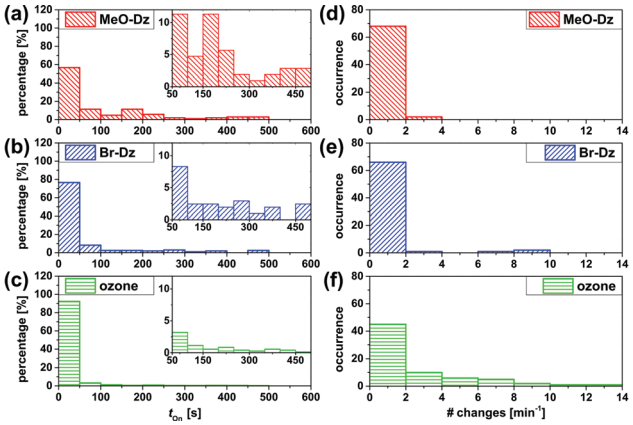

Fig. 7 On times t_{On} of individual E_{11}* emission sites for MeO-Dz doped (a), Br-Dz doped (b) and oxygen doped (c) SWCNTs. Insets in all three histograms show a magnified view of longer-time bins. The right column depicts the number of state changes (On-to-Off, or *vice versa*) for MeO-Dz (d), Br-Dz (e) and oxygen (f) dopant sites.

methoxy-aryl (MeO-Dz) species, blinking is slower and less frequent. These differences can be quantified in two ways: we first define a blinking On or Off event for each individual site by determining a center threshold in the intensity histogram.[45] The intensity threshold allows categorization of the On or Off events and determination of their duration, as extracted from time traces for all the observed E_{11}* emission spots. A histogram of On times t_{On} for each dopant is shown in Fig. 7(a–c). The data also allow us to quantify the blinking rate (Fig. 7(d–f)), defined as the number of change events (On-to-Off, or *vice versa*) per a given time window.

Along the MeO-Dz–Br-Dz–oxygen dopant series, E_{11}* On times are found to progressively decrease, while across the same series, blinking rates are found to increase. Both trends thus indicate an increase in blinking behaviour as one moves from the MeO-Dz to Br-Dz, to oxygen doped tubes. Presence of the bromyl functionality on the Br-Dz dopant creates a more electron-withdrawing species compared to the MeO-Dz moiety. This trend continues with the oxygen dopant and suggests an influence of a progressively stronger permanent dipole associated with each of the dopants, respectively. The observed trend thus suggests a mechanism of dopant charging *via* electrostatic attraction as the blinking origin.

To further explore a possible charging mechanism, we performed DFT calculations of the electrostatic potential in doped carbon nanotubes (as described in the Theoretical modelling section). Contour plots of electrostatic potential for cross-sections sliced across the dopant for each type are shown in Fig. 8(a–c). The plots clearly demonstrate an increasing radial perturbation of the local electrostatic potential in the nanotube across the sequence from MeO-Dz to Br-Dz to oxygen doped structures (Fig. 8(a–c), respectively). The electrostatic potential of the nanotube is perturbed in the vicinity of the defect, and the magnitude of this perturbation correlates with the strength of the permanent dipole moment associated with

Published on 11 November 2015. Downloaded by Los Alamos National Laboratory on 14/12/2016 00:33:04.

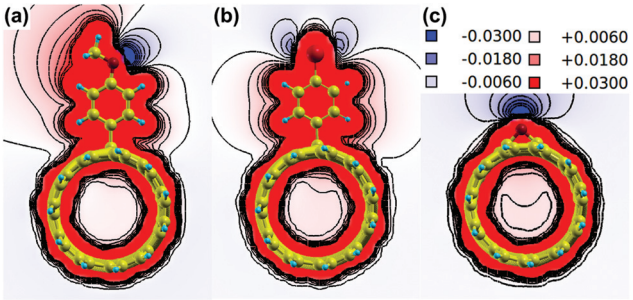

Fig. 8 Calculated electrostatic potential maps of a MeO-Dz doped (a), Br-Dz doped (b) and oxygen doped (c) SWCNT. The color key shown in the inset provides the different values of the isosurfaces (arbitrary units).

the dopant, as well as with the experimentally observed PL blinking behavior. Furthermore, for diazonium species, the perturbation is axially localized near the defect, whereas in ozonated SWCNTs it extends to about 1 nm along the tube axis (see Fig. S6(d–f) ESI†).

The occurrence of such a permanent and increasingly strong electrostatic potential provides a route to increased electrostatic interactions with charged species in solution. The DFT results thus suggest that the dopant acts as an antenna to the environment that attracts external charges. Such charging can significantly enhance non-radiative decay channels,[46,47] thus providing a mechanism for the blinking behavior.

As a final experimental test of the charging hypothesis, we evaluated the effect on blinking behaviour of increasing the concentration of charged species in the nanotube environment. Specifically, we added hydroxide ions by changing sample pH and obtained blinking statistics at pH values of 8, 9, and 12. On-time and blinking rate histograms are shown in Fig. 9 for each of the pH values. Both metrics of blinking behaviour show that, as pH is increased, blinking behaviour also

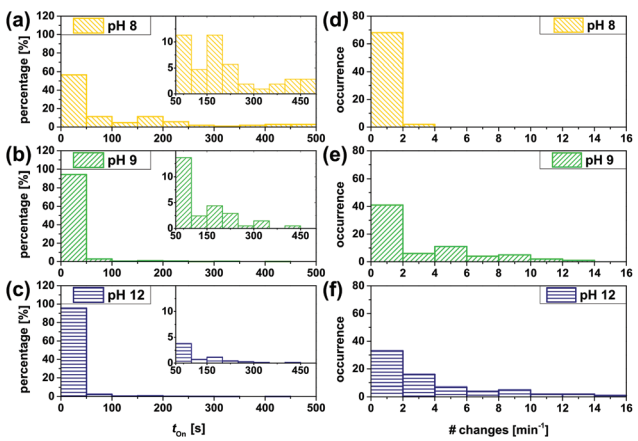

Fig. 9 Average On times for MeO-Dz dopant sites in a pH 8 (a), pH 9 (b) and pH 12 (c) adjusted environment. The number of state changes per minute are shown on the right side column for pH 8 (d), pH 9 (e) and pH 12 (f), respectively.

increases. The results further support our idea that E_{11}* blinking originates from localized interactions of dopant sites with charged species.

As an alternative to the charging mechanism, we have also considered the possibility of blinking occurring as a result of dopant migration on the nanotube surface.[39] For the diazonium species this seems unlikely, as breaking of the sole chemical bond to the surface would result in irreversible loss of the dopant. There is, however, some precedence for migration of oxygen species. Electronic structure theory calculations have indicated that epoxide species can efficiently migrate on graphene surfaces under the influence of an electrostatic potential.[48] Our DFT calculations, however, suggest such migration in our system is unlikely, as a result of thermal barriers to the necessary transition states being too high (see Fig. S5 for details, ESI†). We thus conclude that a charging mechanism remains the most likely origin of E_{11}* blinking.

Conclusions

These PL imaging studies of solitary dopants have been enabled by developing an ability to efficiently introduce dopants and quench sidewall functionalization at a desired level. Such control over manner and extent of doping is essential for expanding the role covalent dopants are poised to take on as a basis for new SWCNT optical behaviours and related applications. By simultaneously showing the correlated behaviour of E_{11} and E_{11}* excitons emitting at different wavelengths, correlated two-color PL imaging is able to address several open questions regarding the ultimate mechanism behind generation of E_{11}* PL emission. Our direct measurements confirm that conversion of E_{11} excitation to E_{11}* emission proceeds *via* initial optical excitation of E_{11}, followed by diffusive transport of the exciton to a dopant site where the exciton is trapped and localized. Subsequent E_{11}* emission from the dopant site is defined by the electronic structure locally introduced by the dopant.

Understanding the observed E_{11}* blinking behaviour is essential for controlling emission uniformity. We have shown that the dopant creates a potential well in the electrostatic potential of the nanotube that may trap free charges, thus turning off emission from the dopant sites. The depth of the well correlates with the magnitude of the permanent dipole associated with the defect site and with the experimentally observed blinking dynamics. Our potential maps are suggestive that dopants may be designed that effectively trap the exciton, while limiting perturbation of the associated electrostatic potentials. It is also useful here to contrast the behaviour observed in the dynamic wet-gel environment of these studies with that found in the solid SiO_2 matrix described by Ma *et al.*[13] that facilitates observation of single photon behaviour. The dynamic aqueous environment of the wet gel allows the charge exchange behind the PL blinking. In contrast, the fixed, solid-state environment does not, thus stabilizing against

 This journal is © The Royal Society of Chemistry 2015

Published on 11 November 2015. Downloaded by Los Alamos National Laboratory on 14/12/2016 00:33:04.

blinking. More importantly, the charging mechanism suggests that moving to non-polar, organic environments may be a fruitful route for further stabilization. Polymer matrices such as those demonstrated in recent works by Strauf and co-workers[15,49,50] may be promising in this regard.

Acknowledgements

This work was supported in part by the Los Alamos National Laboratory (LANL) LDRD program. EHH acknowledges support of a LANL Director's Postdoctoral Fellowship. This work was performed at the Center for Integrated Nanotechnologies, a U. S. Department of Energy, Office of Science user facility.

References

1 E. F. Schubert, *Doping in III-V Semiconductors*, Cambridge University Press, Cambridge, 1st edn, 1993.
2 A. Rogalski, *Appl. Phys. Lett.*, 2003, **93**, 4355.
3 H. Liu, Y. Liu and D. Zhu, *J. Mater. Chem.*, 2011, **21**, 3335.
4 D. Voiry, A. Goswami, R. Kappera, C. d. C. Castro e Silva, D. Kaplan, T. Fujita, M. Chen, T. Asefa and M. Chhowalla, *Nat. Chem.*, 2015, **7**, 45.
5 S. Ghosh, S. M. Bachilo, R. A. Simonette, K. M. Beckingham and R. B. Weisman, *Science*, 2010, **330**, 1656.
6 Y. Piao, B. Meany, L. R. Powell, N. Valley, H. Kwon, G. C. Schatz and Y. Wang, *Nat. Chem.*, 2013, **5**, 840.
7 R. Viswanatha, J. M. Pietryga, V. I. Klimov and S. A. Crooker, *Phys. Rev. Lett.*, 2011, **107**, 067402.
8 C. Kurtsiefer, S. Mayer, P. Zarda and H. Weinfurter, *Phys. Rev. Lett.*, 2000, **85**, 290.
9 P. M. Koenraad and M. E. Flatté, *Nat. Mater.*, 2011, **10**, 91.
10 S. Castelletto, B. C. Johnson, V. Ivády, N. Stavrias, T. Umeda, A. Gali and T. Ohshima, *Nat. Mater.*, 2014, **13**, 151.
11 S. Strauf, P. Michler, M. Klude, D. Hommel, G. Bacher and A. Forchel, *Phys. Rev. Lett.*, 2002, **89**, 177403.
12 M. Koperski, K. Nogajewski, A. Arora, V. Cherkez, P. Mallet, J.-Y. Veuillen, J. Marcus, P. Kossacki and P. Potemski, *Nat. Nanotechnol.*, 2015, **10**, 503.
13 X. Ma, N. F. Hartmann, J. K. S. Baldwin, S. K. Doorn and H. Htoon, *Nat. Nanotechnol.*, 2015, **10**, 671.
14 A. Högele, C. Galland, M. Winger and A. Imamoğlu, *Phys. Rev. Lett.*, 2008, **100**, 217401.
15 W. Walden-Newman, I. Sarpkaya and S. Strauf, *Nano Lett.*, 2012, **12**, 1934.
16 M. S. Hofmann, J. T. Glückert, J. Noé, C. Bourjau, R. Dehmel and A. Högele, *Nat. Nanotechnol.*, 2013, **8**, 502.
17 X. Ma, L. Adamska, H. Yamaguchi, S. E. Yalcin, S. Tretiak, S. K. Doorn and H. Htoon, *ACS Nano*, 2014, **8**, 10782.
18 Y. Miyauchi, M. Iwamura, S. Mouri, T. Kawazoe, M. Ohtsu and K. Matsuda, *Nat. Photonics*, 2013, **7**, 715.
19 M. Iwamura, N. Akizuki, Y. Miyauchi, S. Mouri, J. Shaver, Z. Gao, L. Cognet, B. Lounis and K. Matsuda, *ACS Nano*, 2014, **4**, 67.
20 A. Ishii, M. Yoshida and Y. K. Kato, *Phys. Rev. B: Condens. Matter*, 2015, **91**, 125427.
21 X. Ma, O. Roslyak, J. G. Duque, X. Pang, S. K. Doorn, A. Piryatinski, D. H. Dunlap and H. Htoon, *Phys. Rev. Lett.*, 2015, **115**, 017401.
22 H. Kwon, M. Kim, B. Meany, Y. Piao, L. R. Rowell and Y. Wang, *J. Phys. Chem. C*, 2015, **119**, 3733.
23 N. K. Subbaiyan, A. N. G. Parra-Vasquez, S. Cambré, M. A. Santiago Cordoba, S. E. Yalcin, C. E. Hamilton, N. H. Mack, J. L. Blackburn, S. K. Doorn and J. G. Duque, *Nano Res.*, 2015, **8**, 1755.
24 N. K. Subbaiyan, S. Cambré, A. N. G. Parra-Vasquez, E. H. Hároz, S. K. Doorn and J. G. Duque, *ACS Nano*, 2014, **8**, 1649.
25 J. G. Duque, G. Gupta, L. Cognet, B. Lounis, S. K. Doorn and A. Dattelbaum, *J. Phys. Chem. C*, 2011, **115**, 15147.
26 J. G. Duque, C. E. Hamilton, G. Gupta, S. A. Crooker, J. J. Crochet, A. Mohite, H. Htoon, K. A. Defriend Obrey, A. M. Dattelbaum and S. K. Doorn, *ACS Nano*, 2011, **5**, 6686.
27 C. A. Schneider, W. S. Rasband and K. W. Eliceiri, *Nat. Methods*, 2012, **9**, 671.
28 M. J. Frisch, G. W. Trucks, H. B. Schlegel, G. E. Scuseria, M. A. Robb, J. R. Cheeseman, G. Scalmani, V. Barone, B. Mennucci, G. A. Petersson, H. Nakatsuji, M. Caricato, X. Li, H. P. Hratchian, A. F. Izmaylov, J. Bloino, G. Zheng, J. L. Sonnenberg, M. Hada, M. Ehara, K. Toyota, R. Fukuda, J. Hasegawa, M. Ishida, T. Nakajima, Y. Honda, O. Kitao, H. Nakai, T. Vreven, J. A. Montgomery Jr., J. E. Peralta, F. Ogliaro, M. J. Bearpark, J. Heyd, E. N. Brothers, K. N. Kudin, V. N. Staroverov, R. Kobayashi, J. Normand, K. Raghavachari, A. P. Rendell, J. C. Burant, S. S. Iyengar, J. Tomasi, M. Cossi, N. Rega, N. J. Millam, M. Klene, J. E. Knox, J. B. Cross, V. Bakken, C. Adamo, J. Jaramillo, R. Gomperts, R. E. Stratmann, O. Yazyev, A. J. Austin, R. Cammi, C. Pomelli, J. W. Ochterski, R. L. Martin, K. Morokuma, V. G. Zakrzewski, G. A. Voth, P. Salvador, J. J. Dannenberg, S. Dapprich, A. D. Daniels, Ö. Farkas, J. B. Foresman, J. V. Ortiz, J. Cioslowski and D. J. Fox, Gaussian, Inc., Wallingford, CT, USA, 2009.
29 M. Hanwell, D. Curtis, D. Lonie, T. Vandermeersch, E. Zurek and G. Hutchison, *J. Cheminf.*, 2012, **4**, 17.
30 A. Kokalj, *J. Mol. Graphics Model*, 1999, **17**, 176.
31 S. Kilina and S. Tretiak, *Adv. Funct. Mater.*, 2007, **17**, 3405.
32 C. Lee, W. Yang and R. G. Parr, *Phys. Rev. B: Condens. Matter*, 1988, **37**, 785.
33 C. Peng, P. Y. Ayala, H. B. Schlegel and M. J. Frisch, *J. Comput. Chem.*, 1996, **17**, 49–56.
34 C. Y. Khripin, J. A. Fagan and M. Zheng, *J. Am. Chem. Soc.*, 2013, **135**, 6822.
35 J. A. Fagan, C. Y. Khripin, C. A. Silvera Batista, J. R. Simpson, E. H. Hároz, A. R. Hight Walker and M. Zheng, *Adv. Mater.*, 2014, **26**, 2800.

Published on 11 November 2015. Downloaded by Los Alamos National Laboratory on 14/12/2016 00:33:04.

36 S. Cambré, S. M. Santos, W. Wenseleers, A. R. T. Nugraha, R. Saito, L. Cognet and B. Lounis, *ACS Nano*, 2012, **6**, 2649.
37 O. N. Torrens, M. Zheng and J. M. Kikkawa, *Phys. Rev. Lett.*, 2008, **101**, 157401.
38 H. Htoon, M. J. O'Connell, S. K. Doorn and V. I. Klimov, *Phys. Rev. Lett.*, 2005, **94**, 127403.
39 J. J. Crochet, J. G. Duque, J. H. Werner and S. K. Doorn, *Nat. Nanotechnol.*, 2012, **7**, 126.
40 J. J. Crochet, J. G. Duque, J. H. Werner, B. Lounis, L. Cognet and S. K. Doorn, *Nano Lett.*, 2012, **12**, 5091.
41 A. J. Siitonen, D. A. Tsyboulski, S. M. Bachilo and R. B. Weisman, *Nano Lett.*, 2010, **10**, 1295.
42 C. Georgi, M. Böhmler, H. Qian, L. Novotny and A. Hartschuh, *Phys. Status Solidi B*, 2009, **246**, 2683.
43 H. Deschout, F. C. Zanacchi, M. Mlodzianoski, A. Diaspro, J. Bewersdorf, S. T. Hess and K. Braeckmans, *Nat. Methods*, 2014, **11**, 253.
44 L. Novotny and B. Hecht, *Principles of Nano-Optics*, Cambridge University Press, Cambridge, 2nd edn, 2013, ch. 4.5.
45 C. H. Crouch, O. Sauter, X. Wu, R. Purcell, C. Querner, M. Drndic and M. Pelton, *Nano Lett.*, 2010, **10**, 1692.
46 B. A. Larsen, P. Deria, J. M. Holt, I. N. Stanton, M. J. Heben, M. J. Therien and J. L. Blackburn, *J. Am. Chem. Soc.*, 2012, **134**, 12485.
47 J. G. Duque, L. Oudjedi, J. J. Crochet, S. Tretiak, B. Lounis, S. K. Doorn and L. Cognet, *J. Am. Chem. Soc.*, 2013, **135**, 3379.
48 K. A. Velizhanin, N. Dandu and D. Solenov, *Phys. Rev. B: Condens. Matter*, 2014, **89**, 155414.
49 I. Sarpkaya, Z. Zhang, W. Walde-Newman, X. Wang, J. Hone, C. W. Wong and S. Strauf, *Nat. Commun.*, 2013, **4**, 2152.
50 I. Sarpkaya, E. D. Ahmadi, G. D. Shepard, K. S. Mistry, J. L. Blackburn and S. Strauf, *ACS Nano*, 2015, **9**, 6383.

 This journal is © The Royal Society of Chemistry 2015